Renewable Energy 254 (2025) 123549

Contents lists available at ScienceDirect

Renewable Energy

journal homepage: www.elsevier.com/locate/renene

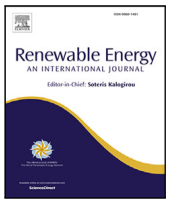

Performance analysis and geometric optimization of bladeless wind turbines using wake oscillator model

Janis Breen, Wrik Mallik *,[1], Sondipon Adhikari[2]

James Watt School of Engineering, The University of Glasgow, Glasgow G12 8QQ, UK

ARTICLE INFO

Keywords:
Bladeless wind turbines
Vortex-induced vibrations
Wake oscillator model

ABSTRACT

This study addresses the critical challenge of optimizing bladeless wind turbines (BWTs) for maximum power extraction while maintaining structural integrity. BWTs represent an innovative approach to wind energy harvesting from vortex-induced vibrations, but their performance characteristics and design constraints remain poorly understood. We present a comprehensive analytical framework combining a nonlinear wake oscillator model with fully coupled elastic-rigid body dynamics to investigate BWT behaviour across a wide parameter space. Unlike previous studies relying on high-fidelity computational modelling or simplified analytical models, our approach enables rapid exploration of complex relationships between BWT geometry, power output, and structural safety. The results reveal a previously unrecognized trade-off: while increasing mast diameter enhances both power extraction and efficiency, maximum power (600 Watts) and peak efficiency (6%) are achieved through distinct geometric configurations. Notably, configurations optimized solely for power output often exceed structural safety limits, while those maximizing efficiency deliver suboptimal power generation. The optimal BWT configuration (mast diameter 0.65 m, length 0.8 m) achieves 460 Watts output while maintaining structural integrity - a significant finding for practical BWT implementation. This study provides the first comprehensive BWT design methodology that balances performance optimization with structural constraints, establishing a foundation for scaling up these promising renewable energy devices.

1. Introduction

Wind energy is rapidly growing as a renewable energy source worldwide. Conventional wind turbines try to convert the mechanical energy of wind into electrical power generation. However, an alternate approach to using wind energy is via energy-harvesting designs based on the aeroelastic vibration of flexible structures. Aeroelastic energy harvesting has been studied over the last two decades by focusing on aeroelastic oscillations of aerofoils [1,2] or vortex-induced vibration (VIV) of cylindrical bluff bodies [3]. Among these, VIV has attracted significant interest in energy harvesting over the last decade, leading to various numerical modelling [4] and experimental research [5,6].

VIV is driven by alternate shedding of vortices from either side of bluff bodies, leading to periodic lift and drag forces and large cross-flow oscillations in flexible structures [7,8]. Under certain flow conditions, the vortex shedding frequency approaches the structure's natural frequency, leading to unstable motion and very large amplitude oscillations. Such behaviour arising from cross-flow VIV of flexible structures is well-known as the lock-in phenomenon [9,10]. Bladeless wind turbines (BWT) have emerged as an innovative concept to harness wind energy by harvesting high-amplitude oscillations of structures in the presence of VIV and lock-in. A BWT effectively behaves as a bluff body placed in a fluid flow that initiates flow separation from its surface, creating vortices in its wake. Thus, BWTs exhibit significant potential for power output within a specific range of wind speeds related to the VIV lock-in range. Notably, research has shown that increasing the oscillation amplitude of a bluff body can widen this capture range [11]. Therefore, designing BWTs with larger oscillation amplitudes can simultaneously increase their power output and operational wind speed range.

Owing to the significant potential of BWTs to extract renewable energy, industrial efforts for harnessing VIV for electricity generation have been undertaken lately on small power output scales (1–100 W) [12]. Furthermore, recent studies have been conducted to assess the potential relationship between BWT power output and design variables such as mast length, weight, and wind speed [13,14]. Recent research has also explored the operational wind speed range of BWTs through a tuning system [15,16]. However, there remains ambiguity

* Corresponding author.
E-mail addresses: Wrik.Mallik@glasgow.ac.uk (W. Mallik), Sondipon.Adhikari@glasgow.ac.uk (S. Adhikari).
[1] Lecturer in Aerospace Engineering.
[2] Professor of Engineering Mechanics.

https://doi.org/10.1016/j.renene.2025.123549
Received 5 February 2025; Received in revised form 2 May 2025; Accepted 21 May 2025
Available online 7 June 2025

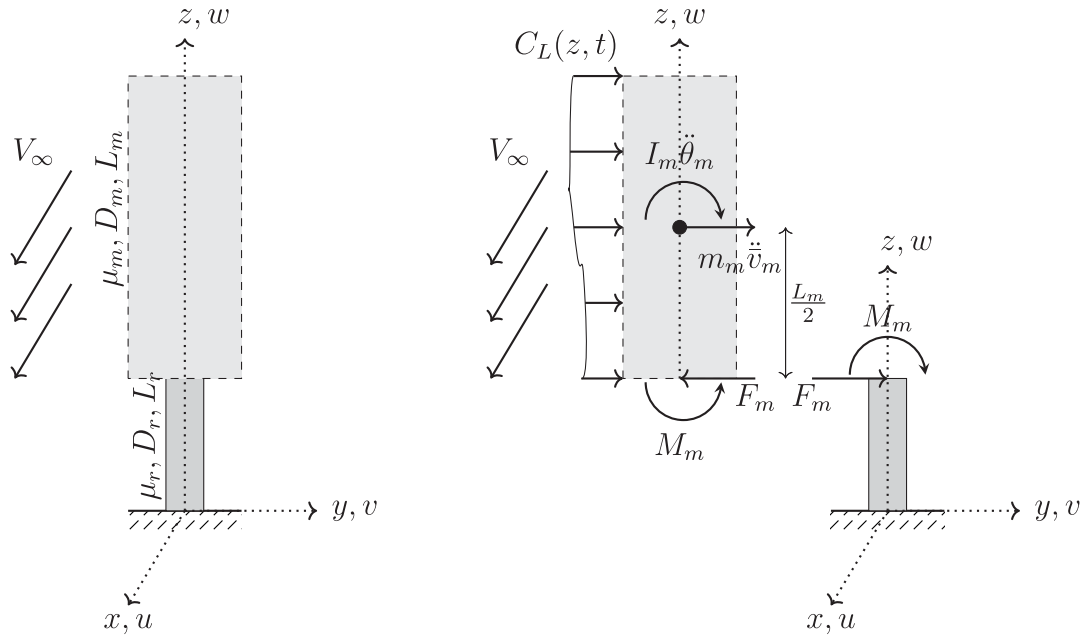

(a) BWT model (b) Free-body diagram of BWT system

Fig. 1. Bladeless wind turbine in the presence of airflow (a) Structural model clamped at the ground, (b) Free-body diagram of BWT system in the presence of aerodynamic and inertial loads.

in the literature regarding BWT efficiency. Recent studies have taken different approaches, with some concentrating on maximizing either the efficiency or input power of BWTs [4,17]. In contrast, others have introduced analytical models for estimating BWT power output or oscillation amplitude [18,19]. Since wind is not a finite resource, it is crucial to determine if maximum efficiency indeed results in maximum BWT power output. Similarly, the question of whether output power can be enhanced for a constant input wind power has yet to be addressed in the literature.

Another gap in the present literature is the lack of a rigorous fluid–structure interaction modelling of BWTs, which can be easily employed to explore BWT parameters and answer various questions on BWT efficiency. Such modelling would significantly accelerate present efforts to scale up existing small-scale BWT models for larger-scale operations (power output 1 kW or more) on offshore sites [20]. Only one recent study has considered a fully coupled elastic-rigid body motion for BWT structure [17] and a nonlinear wake oscillator model for the vortex shedding mechanism from cylindrical BWT structures [21]. However, they consider a relatively old wake oscillator model that cannot be validated at the Reynolds number expected at BWT sites ($Re > 50,000$), and they also do not analyse the power extraction capacity of BWTs. There have been very few recent articles that have explored BWT performance via theoretical modelling and parameter tuning [14,18]. However, they do not consider fluid-elastic coupled models for vortex-induced vibrations [10]. There have been a few studies that attempt high-fidelity computational modelling or experimental analysis of BWT fluid–structure interaction [22]. Such models are ideal for the final validation of expected BWT power extraction or efficiency. However, they are not suited for obtaining key insight into BWT parametric sensitivity and its efficiency owing to the huge computational cost of such modelling.

This research aims to address questions about BWT power output and efficiency by developing a simple numerical model to analyse the physical mechanism of VIVs due to BWTs. The numerical modelling of the complex fluid–structure interaction of VIVs will be based on a nonlinear wake oscillator model [9]. The wake oscillator model can capture the nonlinear dynamics of VIVs and the onset of lock-in, but being a parametric model, it can be tuned easily to explore BWT power generation performance over a wide range of operating conditions and parameters. However, a much more accurate modelling of BWT parameters and a comprehensive analysis of BWT power output are required to obtain valuable conclusions about BWT performance and parameter sensitivity.

This research presents a comprehensive parametric study of BWT power generation capability and efficiency for various BWT geometric parameters. The study considers a fully-coupled elastic-rigid body dynamics modelling to analyse highly rigid BWT masts attached to an elastic BWT base structure. The most recently studied nonlinear wake-oscillator model is employed to couple the unsteady aerodynamics of vortex shedding to the vibrating BWT structure [23]. This enables accurate vortex-induced vibration analysis and identification of lock-in phenomena over a range of free stream velocities and Reynolds numbers. Although the dynamic analysis and power extraction by BWTs have garnered recent research interest, this article presents a comprehensive parametric analysis of BWT geometry based on fully coupled fluid–structure-rigid body dynamic modelling for the first time, to the best of our knowledge. We also provide key insight into the dependence of BWT power extraction on the lock-in phenomena observed by general BWT structures.

2. Dynamic modelling of vortex-induced vibrations in bladeless wind turbines

In this section, we describe the modelling approaches for the BWT's structural dynamics and fluid–structure interaction.

A BWT structure can be represented by a flexible circular rod of diameter D_r, uniform mass distribution μ_r and length L_r attached to the ground, and a rigid hollow circular mast of outer diameter D_m, uniform mass distribution μ_m and length L_m attached to the tip of the rod, without any loss of generality. This is illustrated in Fig. 1(a). Energy harvesting studies [3,24] and lock-in mitigation studies [25,26] around vortex-induced vibration are often studied as a single degree of freedom motion assuming lumped parameter properties matched with first natural frequency of the dominant BWT mode, without any loss of generality for capturing the onset of lock-in phenomenon. However, the structural dynamics of BWT are much more complex and require

accurate coupling of the inertial properties of the BWT mast with those of the vibrating BWT rod. Thus, a continuous structural system is considered with the rod's distributed mass and stiffness.

2.1. Aerodynamic force modelling

A reduced-order wake oscillator model is employed here to represent the aerodynamic loads. Such wake-oscillator models are computationally much less expensive than direct numerical simulations of the Navier–Stokes equations, but provide accurate aerodynamic force predictions in the lock-in region [9,10]. Several types of reduced-order models are available for vortex-induced vibrations [10]; however, coupled system models take into consideration both the evolution of the structural displacement and the dynamics of the wake [23,27]. This study will employ the coupled wake oscillator model proposed by Facchinetti et al. [23]. The wake-oscillator model parameters have been tuned with experiments for the range of Reynolds numbers, $300 < Re < 1.5 \times 10^5$ [23,28], and later validated with direct Navier–Stokes simulations of flow around oscillating cylinders [29]. Although early validations were performed in a hydrodynamic environment, later validation of Facchinetti et al.'s wake oscillator model [23] has also been performed in air with minor changes [30]. This further emphasizes that the model can be used in the present study without loss in generality.

The transverse sectional fluid-dynamic force F_f depends on the lift due to vortex shedding (which depends on the wake dynamics), the flow-induced damping resulting from drag, and the contribution of added mass of the fluid [10,29], as shown below,

$$F_f(z,t) = -\frac{1}{4}\pi\rho_\infty {D_m}^2 \ddot{v} - \frac{1}{2}C_D\rho_\infty D_m V_\infty \dot{v} + \frac{1}{4}C_{L_0}\rho_\infty D_m {V_\infty}^2 p. \tag{1}$$

Here ρ_∞ is the density of the air and V_∞ is the freestream velocity. The direction of the airflow relative to the BWT motion is shown in Fig. 1(a). The unsteady lift can be related to the wake oscillation state p as $C_L(t) = C_{L_0}p(t)/2$. Here, we have neglected the aerodynamic force contribution from the BWT rod as it will have a much smaller diameter than the mast.

A self-excited Van der Pol oscillator governs the wake dynamics,

$$\ddot{p} + \lambda\omega_s\left(p^2 - 1\right)\dot{p} + {\omega_s}^2 p = \frac{\bar{P}}{D_m}\ddot{v}. \tag{2}$$

The wake-oscillator model assumes that the flow is inviscid far from the wake and that there exists a well-formed vortex with a shedding frequency given by $\omega_s = 2\pi St\, V_\infty/D_m$, where St is the Strouhal number of the flow. C_{L_0} is the lift coefficient, which is assumed to have a constant value of 0.3 for the range of Reynolds number stated above [9,31]. For well-developed wakes, the value of C_D is assumed as 1.20. Considering a circular cylinder, and the range of Reynolds number considered here, we can assume that $St = 0.2$ [9,31]. Furthermore, it has been shown that $\lambda = 0.3$ and $\bar{P} = 12$ lead to the best matching of the wake-oscillator predictions with direct numerical simulations of Navier–Stokes equations in the lock-in region [23,29].

2.2. Vortex-induced vibration of BWT

The vortex-induced vibration of the BWT is studied here by separating the BWT system into: (1) the rigid BWT mast, which experiences the aerodynamic loads, and (2) the elastic BWT rod with an equivalent force and moment, F_m and M_m, respectively, at its tip, where the rod and the mast are attached. The free body diagrams of this equivalent system in the presence of aerodynamic and inertial loads are presented in Fig. 1(b).

The structural motion is expressed as a superposition of its free vibration modes ϕ_i,

$$v(z,t) = \sum \phi_i(z)\tilde{v}_i(t), \tag{3}$$

where $\tilde{v}_i$ is the response factor for the i−th mode. Furthermore, based on previous modal superposition of wake oscillator dynamics [17,21], the mode shapes of the wake dynamics state p on a deforming structure can also be approximated by the structural mode shape in the presence of lock-in. In the presence of lock-in, $\omega_s \approx \omega_n$, where ω_n is the natural frequency of the structure. Thus, it is assumed that only the mode shapes of the unsteady lift, which are sufficiently close to the structural modes, have a considerable contribution to the vortex-induced vibration of the system near lock-in. Thus, we have,

$$p(z,t) = \sum \phi_i(z)\tilde{p}_i(t), \tag{4}$$

where $\tilde{p}_i$ is the modal response factor for the i−th mode of unsteady lift.

2.2.1. Undamped free vibration of BWT

Assuming constant properties across the elastic rod and Euler–Bernoulli beam theory, the free vibration of the rod is governed by the following equation of motion,

$$EI\frac{\partial^4 v}{\partial x^4}(z,t) + \mu_r\frac{\partial^2 v}{\partial t^2}(z,t) = 0. \tag{5}$$

Closed-form solutions exist for the system's exact mode shape and natural frequencies. These are obtained using standard methods of modal analysis. The exact mode shapes $\phi_i(z)$ will be used to analyse the vibration of the BWT under aerodynamic loads using Lagrange's equations in the next subsection. A detailed analysis of the first natural frequency and mode shape is provided in Appendix.

For vortex-induced vibration lock-in, often only the first natural mode is important, and the wind velocity required to excite the higher-order modes is beyond the regular wind speeds experienced in most locations. It is thus reasonable to assume that the displacement of the structure and the wake dynamics are governed by the first natural mode of structural vibration.

2.2.2. BWT vibration due to aerodynamic load and proportional damping

The BWT vibration due to aerodynamic loads and dissipation due to damping can be obtained via Lagrange's equations as follows:

$$\frac{d}{dt}\left(\frac{\partial T}{\partial \dot{q}_i}\right) - \frac{\partial T}{\partial q_i} + \frac{\partial \tau}{\partial \dot{q}_i} + \frac{\partial U}{\partial q_i} = Q_i, \tag{6}$$

where T, U and τ are the kinetic energy, potential energy and dissipative energy loss in the elastic rod, respectively. q_i and Q_i are the ith generalized coordinate and force, respectively. T and U are obtained as follows.

$$T = \frac{1}{2}\int_0^{L_r} \mu_r \dot{v}^2(z,t)dz = \frac{1}{2}\sum M_i \dot{\tilde{v}}_i^2(t), \tag{7}$$

and

$$U = \frac{1}{2}\int_0^{L_r} EI{v''}^2(z,t)dz = \frac{1}{2}\sum K_i \tilde{v}_i^2(t), \tag{8}$$

where $M_i = \int_0^{L_r} \mu_r {\phi_i}^2(z)dz$ and $K_i = \int_0^{L_r} EI{\phi_i''}^2(z)dz$. $\tau = \frac{1}{2}\sum C_i \dot{\tilde{v}}_i^2(t)$.

Furthermore, we have $Q_i = \partial W/\partial q_i$, where W is the work done on the rod by the tip force F_m and moment M_m, generated due to the aerodynamic loads and the inertial forces due to the mast's motion. From Fig. 1(b), we have

$$\begin{aligned} W =& F_m v(L_r,t) + M_m\theta(L_r,t) \\ =& F_m\sum \phi_i(L_r)\tilde{v}_i(t) + M_m\sum \phi_i'(L_r)\tilde{v}_i(t). \end{aligned} \tag{9}$$

From Fig. 1(b), F_m and M_m can be obtained as

$$F_m = \int_{L_r}^{L_r+L_m} F_f dz - m_m\ddot{\tilde{v}}_m \tag{10}$$

$$M_m = \int_{L_r}^{L+L_m} F_f(z-L_r)dz - \frac{L_m}{2}m_m\ddot{\tilde{v}}_m - I_m\ddot{\theta}_m. \tag{11}$$

Here, m_m is the mass of the BWT mast and I_m is the moment of inertia of the mast about the x axis. The displacement and rotation of the mast's centre of mass, $\bar{v}_m$ and θ_m, respectively, can be written as,

$$\theta_m = v'(0, L_r) = \sum \phi'_i(L_r)\tilde{v}_i(t)$$
$$\bar{v}_m = v(0, L_r) + \frac{L_m}{2}\theta_m = \sum \phi_i(L_r)\tilde{v}_i(t) + \frac{L_m}{2}\sum \phi'_i(L_r)\tilde{v}_i(t). \quad (12)$$

Substituting Eqs. (7)–(11) in the Lagrange's Eq. (6), we get,

$$M_i\ddot{\tilde{v}}_i + K_i\tilde{v}_i = F_m\phi_i(L_r) + M_m\phi'_i(L_r). \quad (13)$$

As noted earlier, here we will only consider the first natural mode of vibration. Thus, Eq. (13) can be rearranged to form the equation of motion of the system, coupled with the wake dynamics (Eq. (2)) as follows,

$$\left(M + M_a\right)\ddot{\tilde{v}}(t) + \left(C + C_a\right)\dot{\tilde{v}}(t) + K\tilde{v}(t) = \frac{1}{4}C_{L_0}\rho_\infty D_m {V_\infty}^2\gamma\tilde{p}(t), \quad (14)$$

$$\ddot{\tilde{p}}(t) + \lambda\omega_s\left(\beta\tilde{p}^2 - 1\right)\dot{\tilde{p}}(t) + \omega_s^2\tilde{p}(t) = \frac{\bar{P}}{D_m}\ddot{\tilde{v}}(t). \quad (15)$$

Here,

$$M = \int_0^{L_r} \mu_r\phi_i{}^2(z)dz + m_m\left[\phi^2(L_r) + L_m\phi(L_r)\phi'(L_r) + \left(\frac{{L_m}^2}{4} + \frac{I_m}{m_m}\right)\phi'^2(L_r)\right], \quad (16)$$

$$\gamma = \int_{L_r}^{L_r+L_m}\left[\phi^2(L_r) + (z - L_r)\left(2\phi(L_r)\phi'(L_r) + 2(z - L_r)\phi'^2(L_r)\right)\right]dz, \quad (17)$$

$$\beta = \frac{\int_{L_r}^{L_r+L_m} h(z)^3 dz}{\int_{L_r}^{L_r+L_m} h(z)dz}, \quad (18)$$

$$h(z) = \phi(L_r) + (z - L_r)\phi'(L_r), \quad (19)$$

and $C = 2\zeta\omega_n M$, $C_a = \frac{1}{2}\rho_\infty V_\infty D_m C_D\gamma$ and $M_a = \frac{1}{4}\rho_\infty\pi {D_m}^2\gamma$.

The equation of motion of the BWT (Eq. (14)) and the wake oscillator dynamics (Eq. (15)) can be solved by obtaining a state-space representation of the coupled system. Let us assume that

$$x_1 = \tilde{v},\ x_2 = \dot{\tilde{v}},\ x_3 = \tilde{p},\ x_4 = \dot{\tilde{p}}. \quad (20)$$

The coupled dynamical system can now be represented as,

$$\dot{x}_1 = x_2 \quad (21a)$$
$$\dot{x}_2 = -\frac{1}{1 + M_a/M}\omega_n^2 x_1 - \left(\frac{2}{1 + M_a/M}\zeta\omega_n + \frac{C_a}{M + M_a}\right)x_2 \quad (21b)$$
$$+\frac{1}{4}\frac{C_{L_0}\rho_\infty D{V_\infty}^2\gamma}{M + M_a}x_3 \quad (21c)$$
$$\dot{x}_3 = x_4 \quad (21d)$$
$$\dot{x}_4 = -\omega_s^2 x_3 - \lambda\omega_s\left(\beta {x_3}^2 - 1\right)x_4 + \frac{\bar{P}}{D_m}\dot{x}_2 \quad (21e)$$

3. Power generation from vortex-induced vibrations of bladeless wind turbines

The power generated by a BWT depends on the mechanical power in the mast oscillation. Since the electrical power output is directly proportional to the mechanical power generated from vortex-induced vibrations, here we will only focus on the mechanical power output. For an oscillating BWT mast, the instantaneous mechanical power P can be approximated as the total energy E extracted by the BWT system from the free stream. Thus,

$$P = \frac{dE}{dt} = \frac{dW_a}{dt}, \quad (22)$$

where W_a is the total work done by the aerodynamic forces on the BWT system during lock-in. The aerodynamic forces on the BWT mast can be expected to create a force and moment at the BWT rod tip analogous to the equivalent free body systems presented in Fig. 1(b). Thus,

$$W_a = \left(\phi(L_r)\int_{L_r}^{L_r+L_m} F_f dz + \phi'(L_r)\int_{L_r}^{L_r+L_m} F_f(z - L_r)dz\right)\tilde{v}(t). \quad (23)$$

Eq. (22) can be subsequently employed to obtain the extracted power. It is important to note that power extraction depends on both the aerodynamic forces and displacement, and also on their phase difference. Thus, suggestions for power extraction based only on BWT mast tip displacements [17] may not provide accurate results. Furthermore, power extraction based solely on mast tip displacement is not applicable for BWT, where the whole mast's mechanical energy is converted to electrical power.

Since the lift force and the mast velocity are periodic, the mechanical power is better represented by its root mean square (RMS) value obtained over the oscillation period T,

$$P_{\text{RMS}} = \sqrt{\frac{1}{T}\int_0^T P(t)^2 dt}. \quad (24)$$

The RMS pressure is obtained when the flow has developed a fully periodic nature. Its maximum value obtained during the onset of lock-in is thus the critical RMS pressure, $P_{\text{RMS,crit}}$.

The maximum power that could be harnessed from the wind is given as,

$$P_{\text{wind}} = \frac{1}{2}\rho_\infty {V_\infty}^3 D_m L_m, \quad (25)$$

The efficiency of the BWT can be estimated using the assumption that the generator output power is equal to the average mechanical power, since the BWT output power depends on the mechanical power of the mast. Eq. (26) is employed to calculate the efficiency,

$$\eta\,(\%) = 100\left(\frac{P_{\text{RMS,crit}}}{P_{\text{wind}}}\right). \quad (26)$$

4. Results and discussion

4.1. Modal analysis

We consider a BWT with mast material density 1850 kg/m^3 and rod material density 1140 kg/m^3. The rod diameter $D_r = 0.1$ m and rod length $L_r = 0.25$ m. A modal analysis of the BWT structure was performed for a range of BWT mast diameters $D_m = 0.25$ m to $D_m = 0.75$ m and BWT mast length $L_m = 0.8$ to $L_m = 1.6$ m. The modal analysis provided a large range of undamped natural frequencies to be used in the vortex-induced vibration analysis for a comprehensive parametric study of power output and efficiency of BWT operations. The undamped natural frequencies are presented in Fig. 2(a) for the range of BWT mast diameters and lengths considered in this study. The mode shapes for $L_m = 0.8$ m, $D_m = 0.25$ m and for $L_m = 0.8$ m, $D_m = 0.75$ m are presented in Fig. 3. It can be observed that the mast demonstrates only rigid body motion from roughly 0.25 onwards along the normalized distance of the BWT. Although the mode shapes are normalized by their value at $z = L_r$ of the individual BWT masts, some differences are seen in the mast mode shapes for $D_m = 0.25$ m and $D_m = 0.75$ m. This is caused by the different rod tip slope for $D_m = 0.25$ m and $D_m = 0.75$ m as shown in the mast mode shape expression (Eq. (19)).

Larger BWT mast lengths and diameters were not considered here as they would lead to fully rigid BWT dynamical behaviour, not applicable for coupled elastic-rigid BWT structural dynamics modelling considered here. On the other hand, lower BWT mast diameters and lengths would lead to impractical wind speeds and operating conditions, as will be discussed in subsequent results.

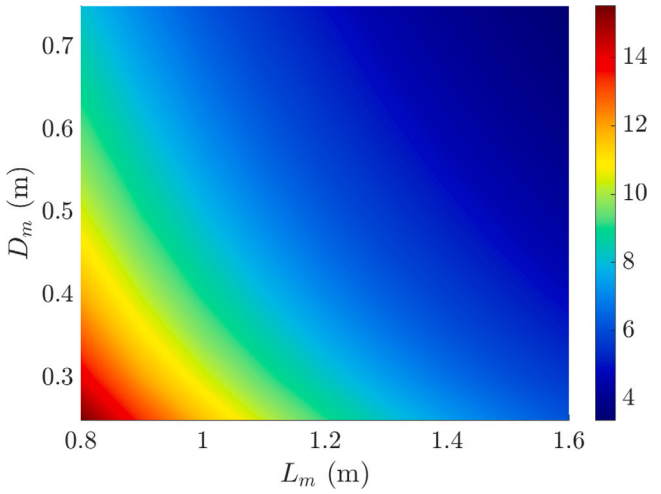

Fig. 2. Undamped natural frequency (Hz.) of the BWT for various mast length L_m and diameters D_m considered.

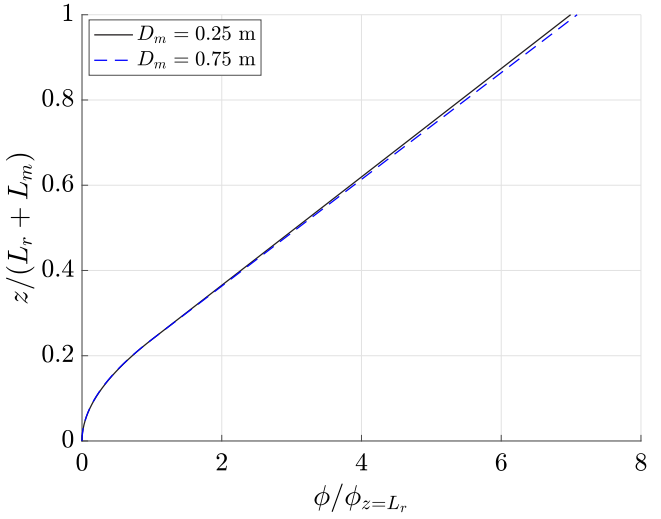

Fig. 3. Normalized mode shapes for $L_m = 0.8$ m and $D_m = 0.25$ m and $D_m = 0.75$ m.

4.2. Vortex-induced vibration analysis

The lock-in phenomenon during vortex-induced vibration is expected near a reduced velocity $V_r = 5$, $V_r = \frac{2\pi V_\infty}{\omega_n D_m}$ as $\omega_s = \omega_n$ at this condition [9,10]. Thus, a reduced velocity range of $V_r = 3.5$ to $V_r = 6.5$ was considered to study the onset of lock-in for the range of BWT mast length and diameters. For each simulation, a time step of $T/32$ was considered for accurate temporal resolution of the response, where T is the period for the undamped natural frequency of the BWT. Each simulation was continued for 150 periods to ensure that a fully developed periodic response could be achieved. Fig. 4 shows the temporal evolution of the BWT rod tip displacement v normalized by the rod diameter D_r, for $L_m = 1.6$ m and $D_m = 0.75$ m. We can observe fully periodic solutions with near-stationary amplitude growth by 150 periods of oscillation. The oscillation amplitude was obtained at $V_r = 5.6$, where the peak displacement amplitude was observed.

The fundamental physics of vortex-induced vibration lock-in can be described by the normalized structural displacement amplitude change with the reduced velocity [9,10]. We thus present the variation of the peak BWT rod tip displacement amplitude A_y, normalized by the rod diameter, with reduced velocities for varying mast length, mass ratio, critical wind velocity and mast diameters. This will provide insight

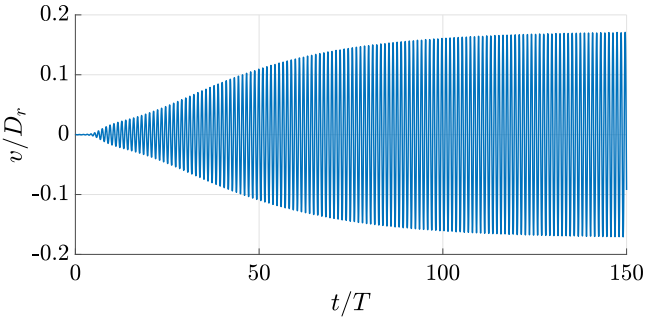

Fig. 4. Evolution of rod tip displacement over several periods of oscillation: $L_m = 1.6$ m and $D_m = 0.75$ m.

into how varying the BWT geometric properties affects the lock-in phenomenon.

Fig. 5(a) presents A_y variation with reduced velocity for $D_m = 0.5$ m. The mass ratio $m_r = (\mu_r L_r/L_m + \mu_m)/(\pi\rho_\infty {D_m}^2/4)$ for these BWT shapes and wind speeds is also provided in Fig. 5(a). A similar set of results for the normalized A_y is presented in Fig. 5(b) for $L_m = 1.2$ m and varying mast diameter. From these two plots, we can draw some general conclusions. First, the rod tip displacement increases with mast diameter and decreases with mast length. Second, the reduced velocity capture range always increases with the mass ratio. However, it is important to note that the true wind speed capture range might be different to the reduced velocity capture range, especially if the critical lock-in velocities change drastically with BWT shape parameters. Thus, we will next look at the relation between the critical wind velocity, where maximum displacement amplitude is expected, and the corresponding BWT shape parameters. It is also important to note that, unlike some previous studies investigating mast tip displacement [17], rod tip displacement is more appropriate for investigating optimum BWT shape parameters. As expected from Fig. 3, the tip displacement will increase linearly with increasing mast length due to rigid body motion and may lead to wrong parameter sensitivity.

Similar to the previous results, the normalized rod tip displacement amplitude is presented over the range of reduced velocities for $D_m = 0.5$ m and varying mast lengths in Fig. 6(a). The critical lock-in velocities V_{crit} for these BWT shapes and wind speeds are also provided in Fig. 6(a). A similar set of results for normalized A_y is presented in Fig. 6(b) for $L_m = 1.2$ m and varying mast diameter. Both these figures show that the rod tip displacement amplitude always increases with V_{crit}. However, the sensitivity of tip displacement to V_{crit} varies with changes in L_m and D_m. It must be noted that $V_{crit} \propto [\omega_n, D_m]$. Thus, V_{crit} will change in a complex manner with changes to BWT mast length and diameter, leading to the complex sensitivity of the tip displacement to a change in BWT mast geometry.

Fig. 7(a) shows the V_{crit} variation with the complete range of L_m and D_m considered here. The result also shows that the shape parameter space limit was selected in such a way that impractical wind speed conditions are not observed. The velocity range thus considered here is roughly 10 m/s to 30 m/s, which is within expected ranges. Fig. 7(b) also shows the critical Reynolds number associated with these varying critical operating conditions and BWT shapes. We can see that for the smallest mast length and largest mast diameters, we reach Reynolds numbers higher than 3×10^5 that are beyond the application limit of the present wake-oscillation. Thus, we will need higher fidelity computational modelling for more accurate prediction of BWT response under such conditions. However, most of the parameter space is within acceptable Reynolds number ranges for the present wake-oscillator model applicability [10,23]. It is important to note that V_{crit} is the highest when the mast diameter is highest and the mast length is smallest. This can be explained by the fact that $V_r = 5$ during lock-in, irrespective of the lock-in velocity. Thus, at critical conditions, the

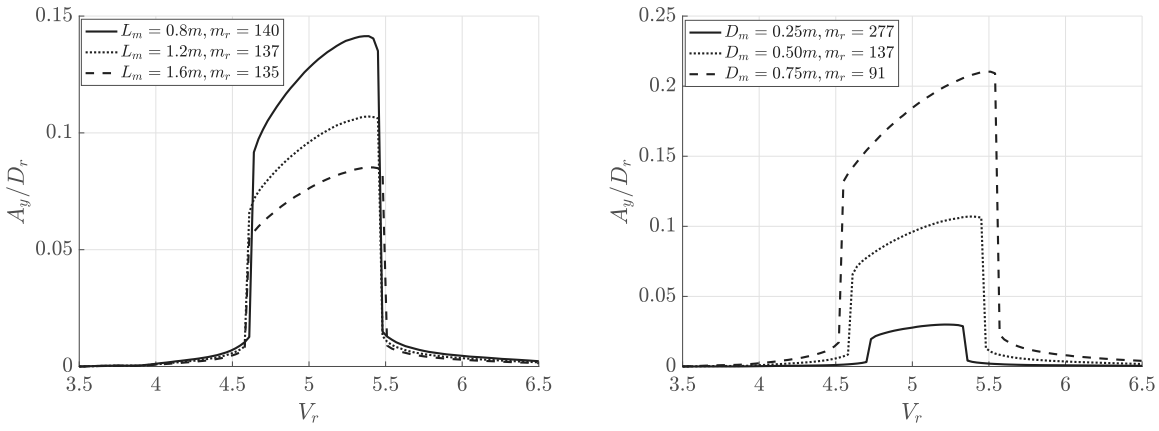

(a) $D_m = 0.5$ m and varying L_m and mass ratio m_r (b) $L_m = 1.2$ m and varying D_m and mass ratio m_r

Fig. 5. Normalized rod tip displacement amplitude A_y/D_r over the reduced velocity V_r range with varying mass ratio m_r as the mast diameter and length are changed.

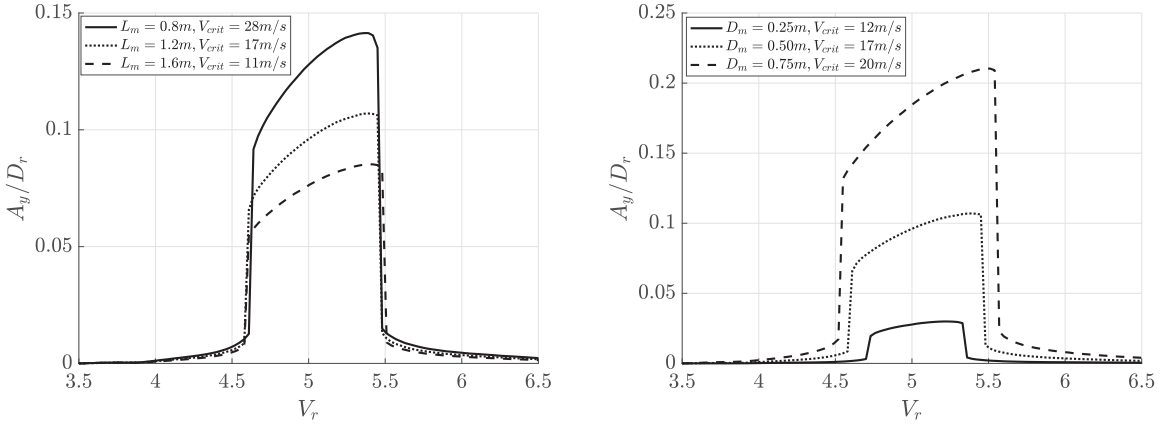

(a) $D_m = 0.5$ m and varying L_m and V_{crit} (b) $L_m = 1.2$ m and varying D_m and V_{crit}

Fig. 6. Normalized rod tip displacement amplitude A_y/D_r over the reduced velocity V_r range with varying critical wind velocity V_{crit} as the mast diameter and length are changed.

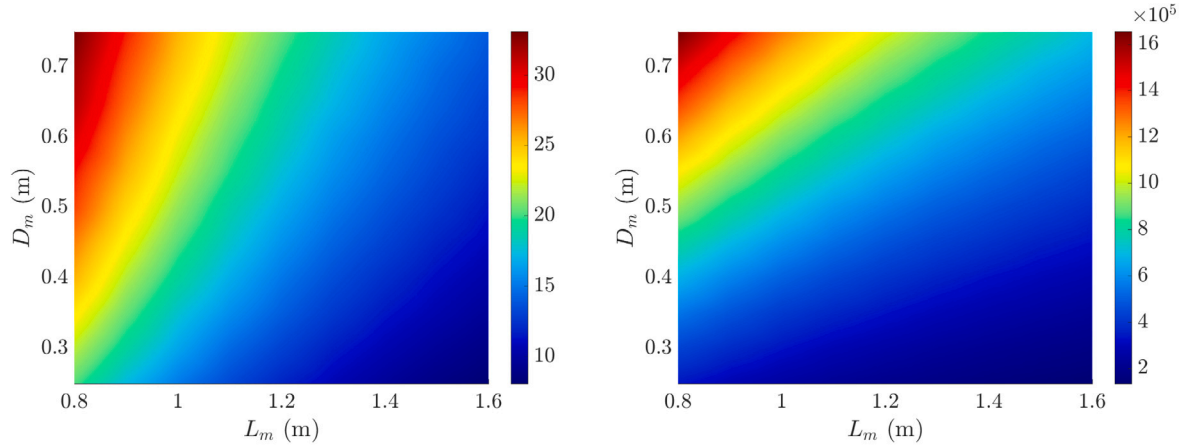

(a) V_{crit} (b) Re_{crit}

Fig. 7. (a) critical wind velocity V_{crit} m/s, and (b) Reynolds number Re_{crit}, with varying mast diameter and length.

wind velocity is directly proportional to the natural frequency and mast diameter. As shown in Fig. 2, the natural frequency is highest at the lowest mast length and frequency. Thus, a combined effect of the frequency and diameter leads to the highest critical velocity at the lowest mast length, but the highest diameter.

4.3. Analysis of output pressure and efficiency

The instantaneous power extracted from the vortex-induced vibrations is presented in Fig. 8(a) at the critical wind speed for $D_m = 0.75$ m and $L_m = 1.6$ m. As noted earlier, a phase difference between the

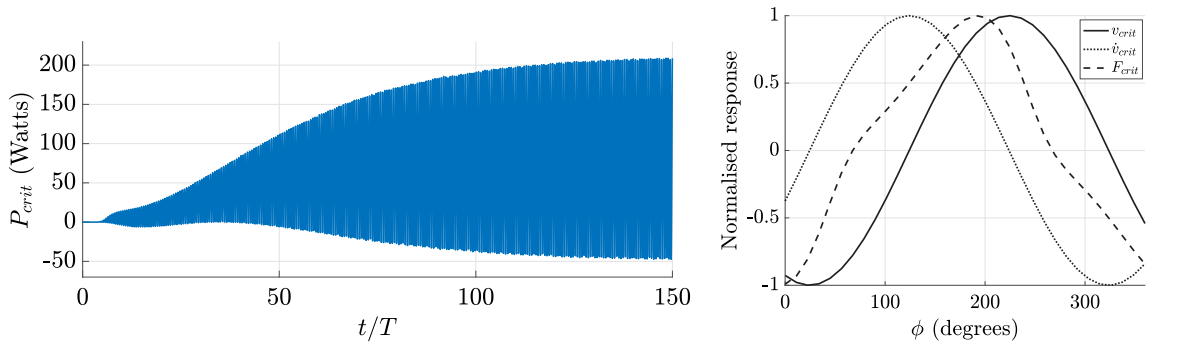

(a) Evolution of critical extractable pressure (b) Phase difference of normalised response

Fig. 8. For $D_m = 0.75$ m and $L_m = 1.6$ m: (a) pressure output from BWT critical vortex-induced vibrations, (b) normalized response of critical displacement, velocity and force.

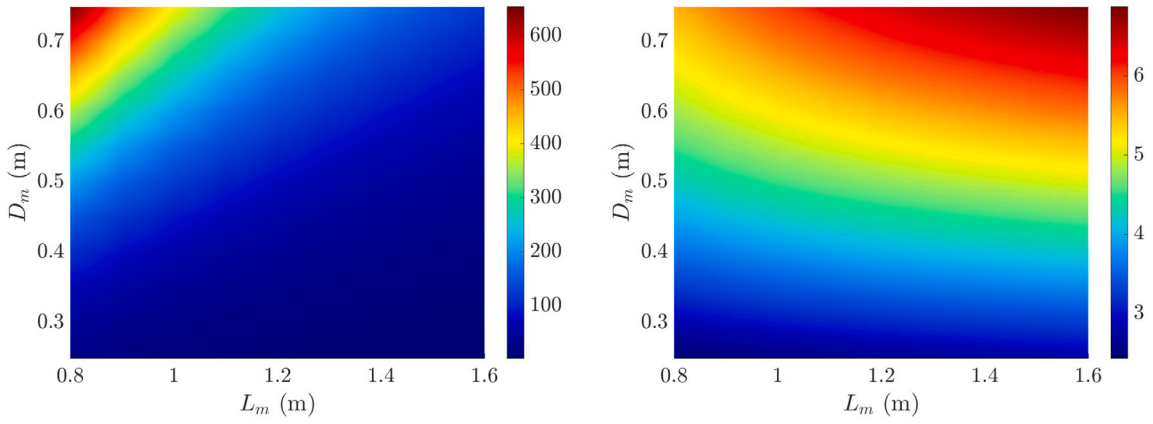

(a) P_{RMS} (Watts) (b) η (%)

Fig. 9. Effect of varying mast diameter and length on (a) RMS of power extracted by the BWT vortex-induced vibrations, and (b) efficiency η.

aerodynamic force and velocity is observed here, which is presented in Fig. 8(b). Such a phase difference depends on the damping ratio of the structure. For a large damping ratio, they are in phase, whereas a phase difference of almost 90° is observed for zero damping ratio. Thus, an RMS value of the instantaneous power is obtained over several cycles after 100 periods of oscillation when fully periodic motion is observed.

The maximum RMS power extracted by the BWT from vortex-induced vibrations for various D_m and L_m is presented in Fig. 9(a). It can be observed that the extracted power always increases with increasing mast diameter and decreasing mast length. This can be easily explained as the maximum RMS power extracted depends on the critical aerodynamic force and displacement, with the force varying as a quadratic function of the critical velocity V_{crit}. As Fig. 9(a) shows, V_{crit} is the maximum for the highest mast diameter and the lower mast length. Overall, a power of over 600 W can be extracted for $L_m = 0.8$ m and $D_m = 0.75$ m, with the present BWT rod configuration and damping properties.

Similar to the RMS power, the efficiency of the BWT wind power extraction is also presented for varying D_m and L_m in Fig. 9(b). We can see that, similar to extracted power, the efficiency of wind power extraction also increases with mast diameter. However, the maximum efficiency is observed for the largest values of L_m. This can be explained by the fact that wind power is a cubic function of the critical wind velocity and would usually increase at one order of critical velocity magnitude higher than the extracted power by BWT vibrations. Thus, a higher increase in critical velocity at a lower mast length implies a higher increase in wind power. This leads to the BWT harnessing greater wind power at lower mast lengths but operating at a lower efficiency.

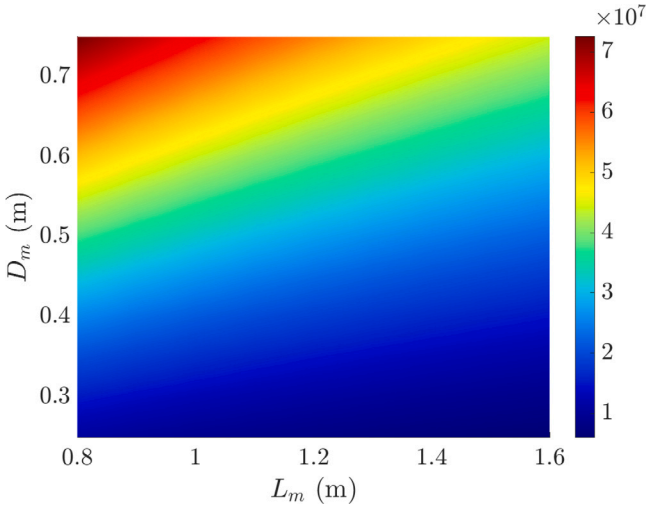

Fig. 10. RMS of rod root bending stress σ_{RMS} (Pa) with varying mast diameter and length.

The condition for the highest power extraction of a BWT would also be the condition for the largest critical displacement and bending stress. Thus, the RMS of the maximum bending stress distribution of the BWT rod at its root is presented in Fig. 10 for varying values of mast length and diameter. The yield stress of the nylon used for modelling the BWT rod lies in the range of 40–60 MPa. Thus, the BWT mast configuration

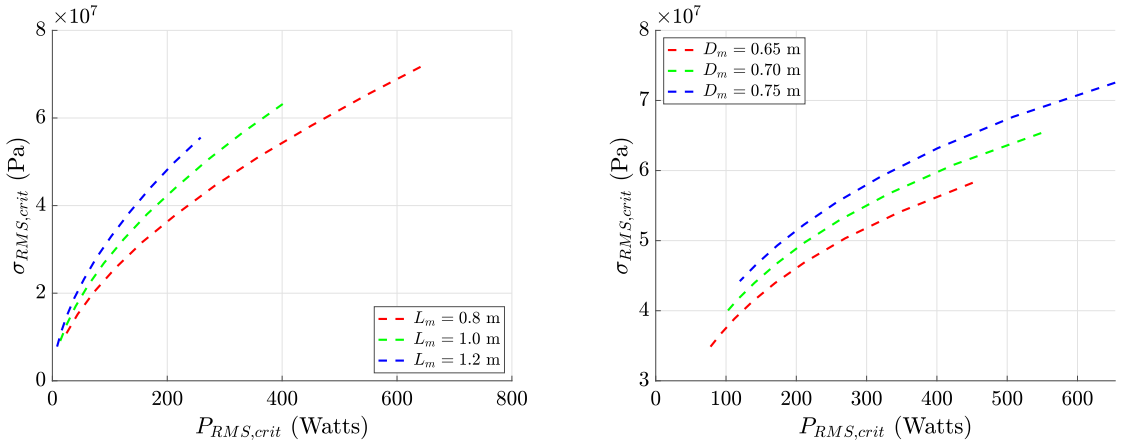

(a) L_m (b) D_m

Fig. 11. Changes in critical RMS root bending stress with critical extracted RMS for (a) selected L_m for all mast diameters, (b) selective D_m with all mast lengths.

of $L_m = 0.8$ m and $D_m = 0.75$ m, providing maximum power, would be structurally unsafe for operation.

Since the BWT mast configuration for maximum power extraction is unsafe from structural bending stress, we now compare how the RMS bending stress of the BWT compares with the maximum power extracted for conditions which lead to the peak responses. Thus, we compare how peak bending stress varies with peak power for the lower L_m values for all mast diameters in Fig. 11(a) and for the highest D_m with all mast lengths considered in Fig. 11(b), respectively. The general takeaway is that power extraction shows large sensitivity to L_m at $L_m = 0.8$ m, with a much lower sensitivity observed for bending stress. On the other hand, both bending stress and power extractions show equal sensitivity to D_m, which is indicated by approximately 45% slope of the plot at $D_m = 0.75$. Furthermore, the sensitivity of both bending stress and power extraction does not change with D_m. This indicates that reducing D_m would be a better approach in general to avoid structural failure from large bending stress without a significant reduction of extracted power. The optimal BWT mast configuration is thus $D_m = 0.65$ m and $L_m = 0.8$ m, as it remains below the highest bending stress threshold of 60 MPa. The maximum possible power extracted is 460 W.

To further emphasize the benefit of selecting the configuration of $L_m = 0.8$ and $D_m = 0.65$ (Fig. 11(b)) we compare it to another structurally safe configuration BWT configuration: $L_m = 1.2$ and $D_m = 0.75$ (Fig. 11(a)). The peak RMS power as well as the lock-in capture range of both these designs are shown in Fig. 12. It can be observed that not only does the BWT mast configuration with $L_m = 0.8$ and $D_m = 0.65$ show much larger peak power, but it also has a much larger capture range.

In summary, this research addresses several critical gaps in the current understanding and design of bladeless wind turbines. First, while previous studies have focused on either efficiency or power optimization in isolation, this work demonstrates the inherent trade-offs between these objectives and provides a unified framework for their analysis. Second, unlike existing approaches that rely on computationally intensive CFD simulations or oversimplified analytical models, this study presents a balanced methodology that captures complex fluid–structure interactions while remaining computationally tractable for broad parametric studies. Third, this research establishes, for the first time, quantitative relationships between BWT geometric parameters and structural safety limits, providing practical design guidelines that consider both performance and reliability. Fourth, through the coupling of a nonlinear wake oscillator model with elastic-rigid body dynamics, this work reveals previously unrecognized dependencies between natural frequency, critical wind speed, and power extraction capacity. Finally, the analytical framework developed here enables rapid exploration of BWT design spaces, making it particularly valuable for scaling up these devices from small-scale demonstrations to utility-scale applications. These contributions collectively establish a foundation for systematic BWT design optimization that balances theoretical rigour with practical implementation constraints.

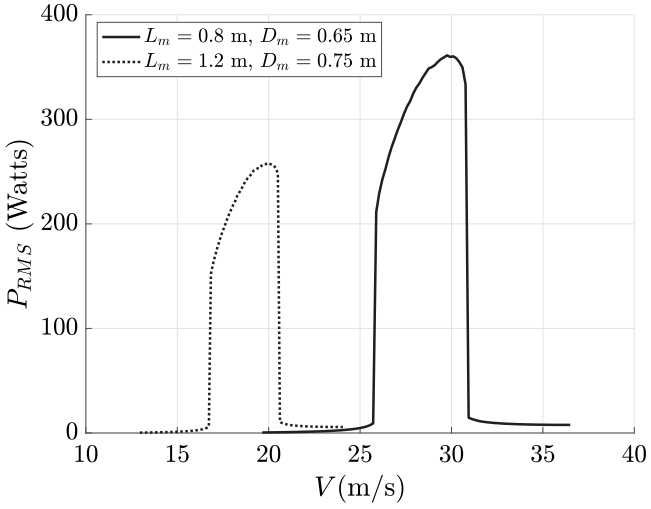

Fig. 12. Capture range of lock-in pressure RMS σ_{RMS} (Pa) for structurally safe BWT mast configurations.

5. Conclusion

This study presents a rigorous analysis of bladeless wind turbine (BWT) performance through a comprehensive framework that couples nonlinear wake oscillator modelling with elastic-rigid body dynamics. The computationally efficient yet accurate modelling framework presented here captures the essential physics of vortex-induced vibrations without requiring intensive CFD simulations. This enabled rapid exploration of the design space and identification of key physical and design insights for BWT.

The investigation encompassed a broad parametric space of BWT geometries, examining their impact on power generation capacity, operational efficiency, and structural integrity. The developed analytical approach successfully identified optimal BWT configurations that balance maximum power extraction with structural safety constraints, demonstrating that a carefully designed BWT can generate up to 460 W while maintaining structural integrity under operational

conditions. The research established the fact that distinct geometric configurations will be obtained for maximizing BWT power output versus efficiency. The results reveal that these objectives cannot be simultaneously optimized, which provides an important insight into BWT design methodology. The study identifies a complex relationship between mast diameter and power generation, where increasing diameter enhances both power and efficiency but may compromise structural stability. These findings have substantial implications for the future development of BWTs as viable renewable energy devices. They can potentially enable the determination of specific geometric parameters that achieve optimal performance within safety limits, providing practical guidance for BWT implementation.

The analytical framework and design guidelines established here provide a foundation for scaling up BWT technology from small-scale demonstrations to utility-scale applications. Future research directions should focus on extending this analysis to arrays of multiple BWTs, investigating interference effects and optimal spacing configurations. Additionally, the wake oscillator model could be enhanced to account for atmospheric turbulence and varying wind conditions, while experimental validation at larger scales would further verify the predicted performance characteristics. The methodology developed here also opens possibilities for investigating advanced materials and adaptive geometric configurations that could further enhance BWT performance and reliability.

CRediT authorship contribution statement

Janis Breen: Writing – original draft, Methodology, Investigation, Formal analysis, Conceptualization. **Wrik Mallik:** Writing – review & editing, Writing – original draft, Validation, Supervision, Project administration, Methodology, Investigation, Formal analysis. **Sondipon Adhikari:** Writing – review & editing, Writing – original draft, Supervision, Project administration, Methodology, Conceptualization.

Declaration of competing interest

The authors declare that they have no known competing financial interests or personal relationships that could have appeared to influence the work reported in this paper.

Appendix. Modal analysis of BWT with classical beam theory

A general solution to Eq. (5) for the elastic BWT rod vibration can be presented as

$$v(z,t) = \phi(z)\tilde{v}(t), \tag{A.1}$$

which can be solved via the separation of variables. A general expression for the spatial component $\phi(z)$ and the temporal component $\tilde{v}(t)$ for free vibration of beams [32] can be written as

$$\phi(z) = A_1 \sin\eta z + A_2 \cos\eta z + A_3 \sinh\eta z + A_4 \cosh\eta z, \tag{A.2}$$

$$\tilde{v}(t) = B_1 \sin\omega_n t + B_2 \cos\omega_n t, \tag{A.3}$$

where the natural frequency of the BWT rod $\omega_n = (\eta L_r)^2 \sqrt{\frac{EI}{\mu_r {L_r}^4}}$.

The free BWT vibration can be considered by analysing the free-body diagram of the flexible cylinder with the inertial forces of the rigid mast being represented by a force-moment couple acting at the tip of the rod as shown in Fig. A.13 with the following boundary conditions:

$$v(0,t) = 0; \quad \frac{\partial v}{\partial z}(0,t) = 0, \tag{A.4}$$

$$EI\frac{\partial^2 v}{\partial z^2}(L_r,t) = -M_m; \quad EI\frac{\partial^3 v}{\partial z^3}(L_r,t) = F_m. \tag{A.5}$$

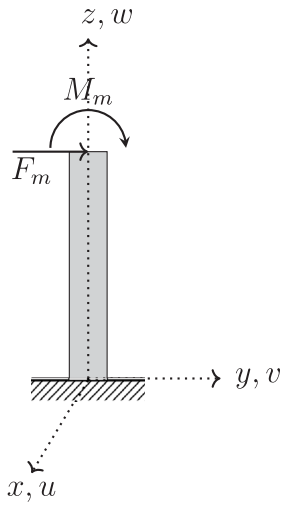

Fig. A.13. Free-body diagram of elastic BWT rod.

The tip force and moment F_m and M_m can be obtained from the inertial forces due to the BWT mast motion as follows,

$$F_m = m_m\ddot{v}_m; \quad M_m = \frac{L_m}{2}m_m\ddot{v}_m + I_m\ddot{\theta}_m. \tag{A.6}$$

Here I_m is the moment of inertia of the mast about the x axis and the displacement and rotation of the mast centre of mass, $\bar{v}_m$ and θ_m, respectively, can be written as,

$$\begin{aligned}\theta_m &= v'(L_r,t) = \phi'(L_r)\tilde{v}(t)\\ \bar{v}_m &= v(L_r,t) + \frac{L_m}{2}\theta_m = \phi(L_r)\tilde{v}(t) + \frac{L_m}{2}\phi'(L_r)\tilde{v}(t).\end{aligned} \tag{A.7}$$

Combining Eqs. (A.5)–(A.7) with Eq. (A.3), we have

$$\begin{aligned}EI\frac{d^2\phi}{dz^2}(L_r) &= {\omega_n}^2\left(\frac{L_m}{2}m_m\left(\phi(L_r) + \frac{L_m}{2}\phi'(L_r)\right) + I_m\phi'(L_r)\right),\\ EI\frac{d^3\phi}{dz^3}(L_r) &= -{\omega_n}^2 m_m\left(\phi_i(L_r) + \frac{L_m}{2}{\phi'}_i(L_r)\right).\end{aligned} \tag{A.8}$$

Eq. (A.2) combined with the essential boundary conditions (Eq. (A.4)) leads to $A_4 = -A_2$ and $A_3 = -A_1$. These equations can be combined with Eq. (A.8) to develop an eigenvalue problem for obtaining the natural frequencies ω_{n_j} and corresponding mode shapes $\phi_j(z)$, for the jth mode of vibration,

$$\begin{bmatrix} Q_3 - e_4Q_2 - e_3Q_1 & Q_4 - e_4Q_3 - e_3Q_2 \\ Q_4 + e_2Q_1 + e_3Q_2 & Q_1 + e_2Q_2 + e_3Q_3 \end{bmatrix}\begin{bmatrix} A_1 \\ A_2 \end{bmatrix} = \begin{bmatrix} 0 \\ 0 \end{bmatrix}, \tag{A.9}$$

where

$$e_1 = \left(\frac{\eta^3 I_m}{\mu_r}\right), \tag{A.10}$$

$$e_2 = \left(\frac{\eta\, m_m}{\mu_r}\right), \tag{A.11}$$

$$e_3 = \eta\frac{L_m}{2}e_2, \tag{A.12}$$

$$e_4 = e_1 + \left(\eta\frac{L_m}{2}\right)^2 e_2, \tag{A.13}$$

and

$$Q_1 = \sin\eta z - \sinh\eta z, \tag{A.14}$$

$$Q_2 = \cos\eta z - \cosh\eta z, \tag{A.15}$$

$$Q_3 = -\sin\eta z - \sinh\eta z, \tag{A.16}$$

$$Q_4 = -\cos\eta z - \cosh\eta z. \tag{A.17}$$

Data availability

No data was used for the research described in this article.

References

[1] T. Sarpkaya, A critical review of the intrinsic nature of vortex-induced vibrations, J. Fluids Struct. 19 (2004) 389–447.

[2] Z. Peng, Q. Zhu, Energy harvesting through flow-induced oscillations of a foil, Phys. Fluids 21 (12) (2009).

[3] A. Abdelkefi, Aeroelastic energy harvesting: A review, Internat. J. Engrg. Sci. 100 (2016) 112–135.

[4] A. Barrero-Gil, S. Pindado, S. Avila, Extracting energy from vortex-induced vibrations: A parametric study, J. Appl. Math. Model. 36 (2012) 3153–3160.

[5] A. Abdelkefi, M. Hajj, A. Nayfeh, Piezoelectric energy harvesting from transverse galloping of bluff bodies, Smart Mater. Struct. 22 (1) (2012) 015014.

[6] Y.J. Lee, Y. Qi, G. Zhou, K.B. Lua, Vortex-induced vibration wind energy harvesting by piezoelectric MEMS device in formation, Sci. Rep. 9 (1) (2019) 20404.

[7] J.H. Gerrard, The mechanics of the formation region of vortices behind bluff bodies, J. Fluid Mech. 25 (2) (1966) 401–413.

[8] R. Bishop, A. Hassan, The lift and drag forces on a circular cylinder in a flowing fluid, Proc. R. Soc. Lond. 272 (1368) (1963) 32–50.

[9] R.D. Blevins, Flow-Induced Vibration: Second Edition, Krieger Publishing Company, 2001, Chapter 3.

[10] M.P. Païdoussis, S.J. Price, E. De Langre, Fluid-Structure Interactions: Cross-Flow-Induced Instabilities, Cambridge University Press, 2010.

[11] P.W. Bearman, Vortex shedding from oscillating bluff bodies, Annu. Rev. Fluid Mech. 16 (1984) 195–222.

[12] M.M. Bernitsas, K. Raghavan, Y. Ben-Simon, E.M.H. Garcia, VIVACE: A new concept in generation of clean and renewable energy from fluid flow, J. Offshore Mech. Arct. Eng. 130 (2008).

[13] C.M. Asre, V.K. Kurkute, N.J. Kanu, Power generation with the application of vortex wind turbine, Mater. Today: Proc. 56 (2022) 2428–2436.

[14] I. Bahadur, Dynamic modelling and investigation of a tuneable vortex bladeless wind turbine, Energies 15 (6773) (2022) 1–18.

[15] D.J.Y. Villarreal, VIV Resonant Wind Generators, Tech. rep., Vortex Bladeless S.L., 2018.

[16] E. González-González, D.J. Yáñez, S. Del Pozo, S. Lagüela, Optimizing bladeless wind turbines: Morphological analysis and lock-in range variations, Appl. Sci. 14 (7) (2024) http://dx.doi.org/10.3390/app14072815, URL https://www.mdpi.com/2076-3417/14/7/2815.

[17] A. Chizfahm, E.A. Yazdi, M. Eghtesad, Dynamic modelling of vortex-induced vibration wind turbines, J. Renew. Energy 121 (2018) 632–643.

[18] A.M. Elsayed, M.B. Farghaly, Theoretical and numerical analysis of vortex bladeless wind turbines, J. Wind. Eng. 46 (5) (2022) 1408–1426.

[19] C. Chen, J. Zhou, F. Li, D. Gong, Nonlinear vortex-induced vibration of wind turbine towers: Theory and experimental validation, Mech. Syst. Process. 204 (2023) 1–18.

[20] J.C. Cajas, G. Houzeaux, D.J.Y. nez, M. Mier-Torrecilla, SHAPE Project Vortex Bladeless: Parallel multi-code coupling for fluid-structure interaction in wind energy generation, Tech. rep., Barcelona Supercomputing Center, 2020.

[21] R.A. Skop, S. Balasubramanian, A new twist on an old model for vortex-excited vibrations, J. Fluids Struct. 11 (4) (1997) 395–412.

[22] A. Younis, Z. Dong, M. ElBadawy, A. AlAnazi, H. Salem, A. AlAwadhi, Design and development of bladeless vibration-based piezoelectric energy–harvesting wind turbine, Appl. Sci. 12 (15) (2022) 7769.

[23] M.L. Facchinetti, E. De Langre, F. Biolley, Coupling of structure and wake oscillators in vortex-induced vibrations, J. Fluids Struct. 19 (2) (2004) 123–140.

[24] H. Dai, A. Abdelkefi, L. Wang, Piezoelectric energy harvesting from concurrent vortex-induced vibrations and base excitations, Nonlinear Dynam. 77 (2014) 967–981.

[25] H. Dai, A. Abdelkefi, L. Wang, W. Liu, Time-delay feedback controller for amplitude reduction in vortex-induced vibrations, Nonlinear Dynam. 80 (2015) 59–70.

[26] W. Mallik, S. Santra, Mitigation of vortex-induced vibration lock-in using time-delay closed-loop control, Nonlinear Dynam. 100 (2020) 1441–1456.

[27] W. Iwan, R. Blevins, A model for vortex-induced oscillation of structures, J. Appl. Mech. 41 (3) (1974) 581–586.

[28] M. Keber, M. Wiercigroch, Dynamics of a vertical riser with weak structural nonlinearity excited by wakes, J. Sound Vib. 315 (3) (2008) 685–699.

[29] R. Violette, E. De Langre, J. Szydlowski, Computation of vortex-induced vibrations of long structures using a wake oscillator model: comparison with DNS and experiments, Comput. Struct. 85 (11–14) (2007) 1134–1141.

[30] H. Dai, A. Abdelkefi, L. Wang, Theoretical modeling and nonlinear analysis of piezoelectric energy harvesting from vortex-induced vibrations, J. Intell. Mater. Syst. Struct. 25 (14) (2014) 1861–1874.

[31] M.S. Pantazopoulos, Vortex-induced vibration parameters: critical review, Am. Soc. Mech. Eng. N. Y. NY (United States) (1994).

[32] D. Shabana, Vibration of Discrete and Continuous Systems, Mechanical Engineering Series, Springer, 2019, Chapter 4.